Supporting Information for

"Development of a High-Resolution Laser Absorption Spectroscopy Method with Application to the Determination of Absolute Concentration of Gaseous Elemental Mercury in Air"

Abneesh Srivastava and Joseph T. Hodges

Chemical Sciences Division, National Institute of Standards and Technology, 100 Bureau Drive, Gaithersburg, Maryland 20899-8393, United States
Corresponding author: Abneesh Srivastava, email: abneesh.srivastava@nist.gov

Table of Contents

S1. Simulation of mercury absorption spectrum

Table S1.I. Summary of mercury $6\ ^1S_0 \leftarrow 6\ ^3P_1$ transitions, masses, isotopic abundances, absolute transition frequencies, uncertainties, degeneracy ratios and unweighted and isotopically weighted intensities. All frequencies are based on the absolute position of the 198 amu isotope (line 2) given by Kramida (2011)[1] and the positions and uncertainties relative to this line from Schweitzer (1963)[2] with the exception of the relative position of line 1 (196 amu isotope) which is taken from Bitter (1962)[3]. Intensities are based on $A_{21} = 8.41 \pm 0.28 \times 10^6\ s^{-1}$ assumed for all transitions. Note that the sum of the isotopically weighted intensities is $S_{tot} = 6.463\times10^{-8}\ m^2/s$ and is nearly independent of the relative isotopic abundances.

i	label	m_i	χ_i	ν_i (THz)	$u(\nu_i)$ (MHz)	$g_{2,i} / g_{1,i}$	$S_{i,unweighted}$ (10^{-8} m^{2}s)	$S_{i,weighted}$ (10^{-8} m^{2}s)
1	196	195.96581	0.0015	1181.5598941	120	3	6.463	0.00969
2	198	197.96674	0.1004	1181.5557869	3.6	3	6.463	0.6489
3	199A	198.96825	0.1694	1181.5403779	13.4	1	2.154	0.3649
4	199B	198.96825	0.1694	1181.5625143	7.8	2	4.308	0.7298
5	200	199.96825	0.2314	1181.5509816	5.8	3	6.463	1.4955
6	201a	200.97028	0.1317	1181.5411283	10.5	3/2	3.231	0.4256
7	201b	200.97028	0.1317	1181.5551106	4.5	1	2.154	0.2837
8	201c	200.97028	0.1317	1181.5626591	15.7	1/2	1.077	0.1419
9	202	201.97062	0.2974	1181.5456851	5.8	3	6.463	1.9220
10	204	203.97347	0.0682	1181.5404745	13.4	3	6.463	0.4408

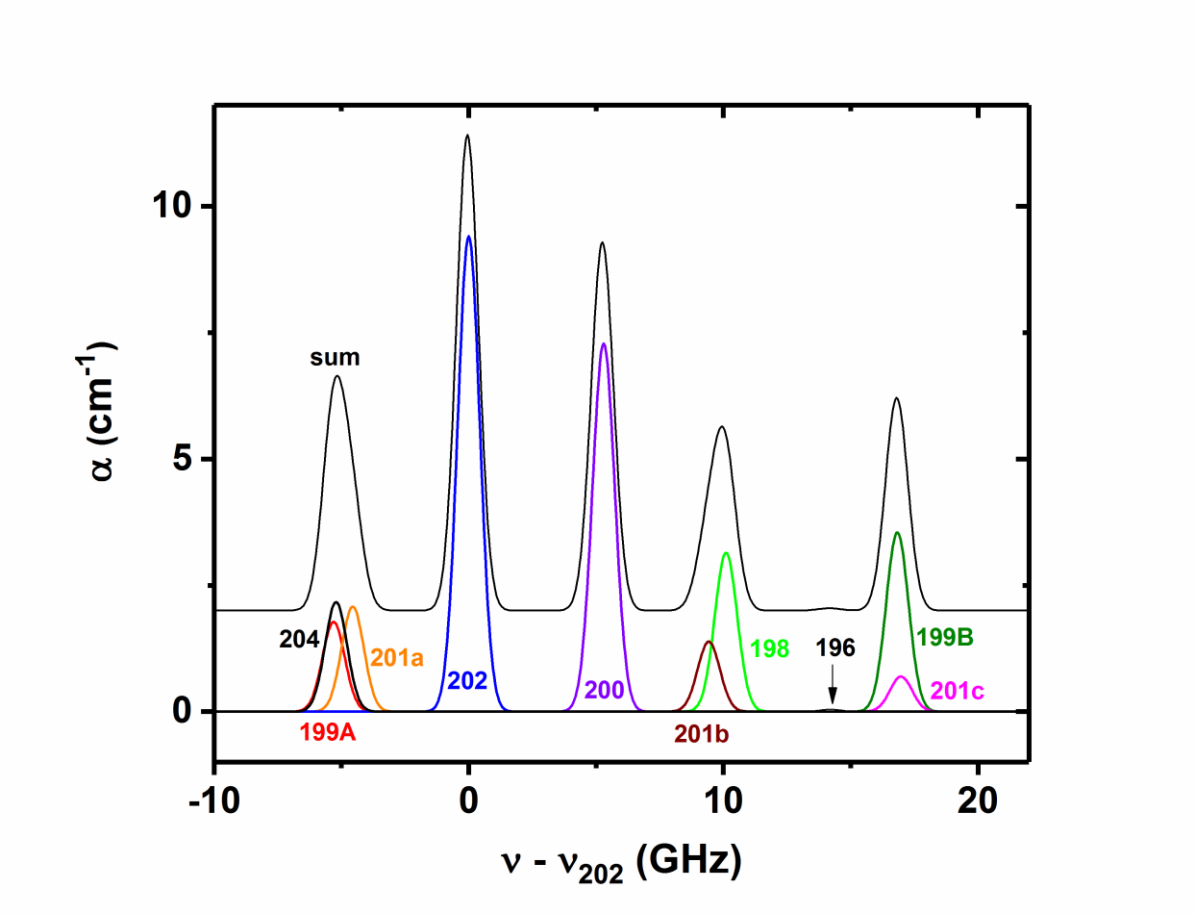

Figure S1.1. Simulated spectrum for pure mercury vapor at T = 296 K with indicated transitions. Natural isotopic abundance is assumed for the constituent isotopes. Note the composite spectrum is offset by 2 cm^{-1} along the vertical axis for clarity.

S2. Saturation and photoreaction effects

We measured a series of spectra for all three samples to identify the thresholds below which intensity saturation and photoreaction effects (for the Hg-Air samples) would be eliminated. Typically, the laser beam power incident on the sample cells was less than approximately (0.1 μW) and was adjusted to avoid obvious saturation using neutral density filters. To quantify the

onset of saturation, which occurs when there is significant perturbation to the equilibrium thermal population of the mercury atoms in the ground state caused by laser pumping, we measured $n_{Hg}A_{21}l$ for the Hg-only, Hg-Air, and Hg-N_2 samples as a function of maximum incident laser intensity, I_i. In this simplified analysis of saturation, we consider only the peak intensity of the beam, neglecting the transverse profile and strong beam attenuation caused by absorption for the Hg sample. We estimated the peak beam intensity assuming a Gaussian beam profile and from the measured beam power, P_t, and effective $1/e^2$ radius, $w = \sqrt{w_x w_y}$ as $I_i = 2P_t/(\pi w^2)$, where w_x, w_y are the measured beam radii along two orthogonal directions. We considered peak intensities ranging from 10^{-2} Wm^{-2} to 500 Wm^{-2}, which widely bracket the expected saturation intensity of the mercury transitions for the Hg-only sample given by $I_{sat} = \frac{\pi}{3}\frac{h\nu}{\lambda^2}A_{21} = 107.1\,W/m^2$. The results for all three samples are summarized in Fig. S2.1, in which the quantity $\eta_{sat}(I_i) = n_{Hg}(I_i)/n_{Hg,0}$ is plotted against I_i, where $n_{Hg,0}$ is the mercury number density in the limit of 0 beam intensity. As expected, for the pure Hg samples, η_{sat} exhibits a strong dependence on intensity for $I_i > I_{sat}$. Assuming that saturation is consistent with inhomogeneously broadened (Doppler profiles) then $\eta_{sat}(I_i) = 1/\sqrt{1 + I_i/I_{sat}}$. We fit this expression to the Hg sample data treating $n_{Hg,0}$ and a factor scaling the measured effective radius of the Gaussian-profile laser beam as fitted parameters. Based on the fitted saturation curve and a typical experimental intensity of 0.007 Wm^{-2} (indicated by the vertical dashed line, and corresponding to saturation parameter, $I_i/I_{sat} = 6.5\times10^{-5}$), we estimate that relative amount of saturation was less than 3.5×10^{-5}. We also estimated the saturation broadening[4] of the Doppler-broadened lines to be less than 30 kHz at our typical experimental intensity. Also, at these

fluences, the temperature rise in the cell caused by absorption of the laser beam was calculated to be less than 1 mK and therefore was neglected.

Figure S2.1 shows that the Hg-N_2 samples do not saturate at the laser intensities considered here. This is to be expected given that relaxation of the mercury atoms from the excited state is promoted by the collisions with the N_2 bath gas. In this regime, the line profiles are mostly homogeneously broadened, and the relaxation rate is dominated by the foreign pressure

broadening, giving a relaxation rate that exceeds A_{21} by more than three orders of magnitude. In contrast to the Hg-N_2 results, the absorption data in Fig. S2.1 for Hg-Air samples show a significant reduction in absorption as the beam intensity increases. We attribute this trend to well-studied photoreaction effects[5,6] occurring via the quenching of Hg excited state. Unlike intensity saturation in the Hg-only sample, the reduction in measured Hg number density for the Hg-Air sample was time dependent and was a manifestation of slow, photo-induced reactions that lead to the formation of HgO per

$$Hg + 2O_2 \overset{253.7nm}{\rightarrow} HgO + O_3$$

This effect was eliminated by operating at intensities below about 10^{-2} Wm^{-2}. The reported photoreaction threshold is also well below the 253.7 nm ultraviolet photo-deposition results of Granite *et al.*[6,7] for Hg in oxygen-nitrogen mixture near room temperature in a quartz photoreactor under flowing conditions (1 $mWcm^{-2} \equiv 10$ Wm^{-2}, with 81.5% mercury capture). Furthermore, we expect that in an open system, where Hg-Air sample continuously enter and leave the sample volume, significantly higher beam intensities could be accommodated without encountering this complication. Additionally, the invariance of the number density at low

intensities (10^{-2} Wm^{-2}) across our sample-triad suggests no detectable anomalous surface effects, under of experimental uncertainty.

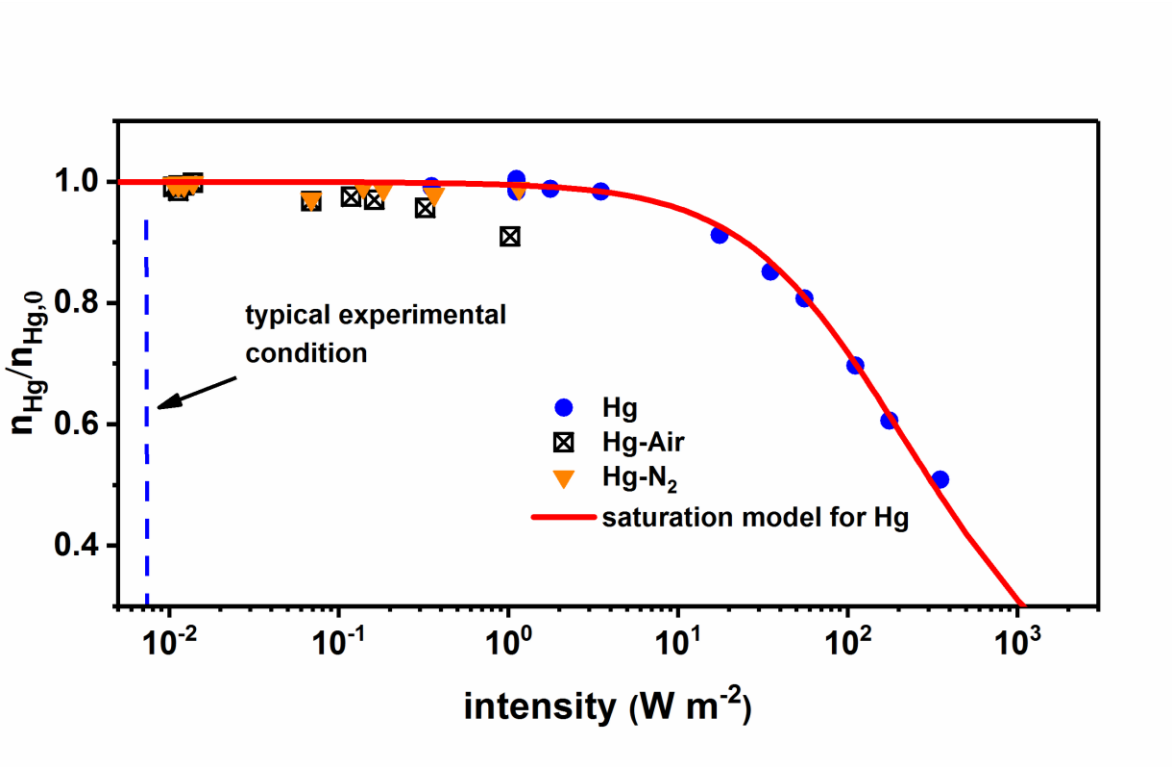

Figure S2.1. Dependence of integrated absorption on laser intensity for Hg, Hg-N_2 and Hg-Air samples. The red line represents the expected dependence for the Hg sample based on inhomogeneous broadening and assuming $I_{sat} = 107.1 \mathrm{W/m^2}$. We note that the Hg-Air case exhibits an intensity dependence because of photothermal induced oxidation of the elemental mercury, not because of intensity saturation. All other data reported in the present study correspond to laser intensities near that indicated by the blue line, in which saturation effects are negligible.

S3. Effect of multiple reflections and cell orientation

We computed a modification to the geometrical pathlength, to account for potential multiple reflections between cell walls. This correction, which assumes incoherent addition of the reflected fields and was estimated in terms of the effective reflectivity of the fused silica windows (equal to 0.08 for two surfaces) at 254 nm, leads to an effective path length that is

larger by (0.2 to 0.4) % compared to the geometrical, single-pass value. Also, the sensitivity of pathlength to cell orientation relative to the incident beam was evaluated and optimized to result in the minimum path length. The sensitivity of path length to cell orientation gives a 0.1 % over-estimation of path length for ±3° spread relative to its minimum value.

S4. Uncertainty analysis

Here we provide equations used to compute the individual and combined relative standard uncertainty for the Hg vapor mass concentration reported in the main article. The resulting contributions with a description of the uncertainty terms are tabulated in Table S4.I.

Least-squares analysis of the measured spectra (using equations 1,3 and 6 of main article) yielded the product, $m = n_{Hg} A_{21} \mathrm{l}$ as a fit parameter along with its associated fit uncertainty. The values of isotopic abundance, χ_i and temperature T were kept fixed during a given data spectrum fit analysis. For the isotopic abundance, χ_i the fit input value was set to the terrestrial natural abundance and for temperature the input was set to its measured value during the spectral scan. In this fashion, the "*m*" value is computed for each spectral scan and its variability across the measurement dataset obtained. The value of n_{Hg} is subsequently calculated for each "*m*" value using the known path length, *l* and spontaneous emission Einstein coefficient, A_{21} value. Both path length and spontaneous coefficient have uncertainties (Type B) which will contribute to the uncertainty in *n* derived from *m.*

The fit parameter "*m*" for each spectrum requires knowledge of χ_i and T as indicated above. However, both χ_i and T have uncertainties that will influence the value of the spectral fit

parameter *m* and hence the derived value of *n.* In addition, the uncertainty in temperature will contribute to an uncertainty in *n* due to vapor pressure-temperature dependence.

We therefore construct a combined uncertainty that includes the effect of A_{21}, *m*, *T,* l , χ_i using propagation of errors as,

$$u(n_{Hg}(T)) = \sqrt{\left(\frac{\partial n}{\partial \mathrm{l}}\right)^2 u^2(\mathrm{l}) + + \left(\frac{\partial n}{\partial A_{21}}\right) u^2(A_{21}) + \left(\frac{\partial n}{\partial m}\right)^2 u^2(m) + \left(\frac{\Delta m}{\Delta \chi_i}\right)^2 u^2(\chi_i) + \left(\frac{\Delta m}{\Delta T}\right)^2 u_{cal}{}^2(T) + \left(\frac{\partial n}{\partial T}\right)^2 u_{cal}{}^2(T)} \qquad \text{(S1)}$$

The sensitivity of the fit parameter, "$m = nA_{21}l$" to uncertainty in isotopic abundance, $u(\chi_i)$, was estimated by computing its values for varying χ_i. The constraint of $\sum_i \chi_i = 1$ was imposed. Here $u(\chi_i)$ corresponds to the reported standard uncertainties in the terrestrial natural isotopic abundance values of mercury. This analysis was found to produce $\left(\frac{\left(\frac{\Delta m}{\Delta \chi_i}\right)}{m}\right)_{A_{21},l} u(\chi_i)\% = 0.2$. For fixed A_{21}, l values one gets the relationship $\left(\frac{\Delta m}{m}\right)_{A_{21},l}\% = \left(\frac{\Delta n}{n}\right)\%$. Hence the contribution of the isotopic abundance uncertainty to number density values, *n*, derived from the fit parameter, *m* is $\left(\frac{\left(\frac{\Delta n}{\Delta \chi_i}\right)}{n}\right)_{A_{21},l} u(\chi_i)\% = 0.2$.

The sensitivity of the fit parameter *m* to temperature was also evaluated. For this the spectral fits were calculated to generate a series of fit values of the quantity "*m"* as a function of T. The resulting contribution $\left(\frac{\frac{\Delta m}{\Delta T}}{m}\right) u_{cal}(T)\%$ was found to be negligible. This dependence reflects the

sensitivity to Doppler width to temperature. Here u_{cal} refers to the Type B uncertainty in temperature associated with its calibration.

The sensitivity coefficient $\frac{\partial n}{\partial T}$ is derived using the Wagner-type equation for the vapor pressure-temperature correlation function, $\ln\left(\frac{p}{p_c}\right)=\frac{T_c}{T}\sum_{i=1}^{6}a_i\tau^{e_i}$ provided by Huber et al. and the ideal gas law relationship, $n=\frac{p}{k_BT}$. Here a_i represents the vapor pressure correlation function fitted parameters, e_i represents the exponents with values, $\tau = T/T_c$ in which T_c is the critical point of mercury and k_B is the Boltzmann constant. The resulting expression for $\frac{\partial n}{\partial T}$ can be written as

$$\frac{\partial n}{\partial T}=\frac{1}{k_BT}\left[\frac{\partial p}{\partial T}-\frac{p}{T}\right], \tag{S2}$$

where

$$\frac{\partial p}{\partial T}=-\frac{p}{T}\left[\ln\left(\frac{p}{pc}\right)+\sum_{i=1}^{6}a_ie_i\tau^{e_i-1}\right] \tag{S3}$$

This analysis gives, $\frac{\partial n(T)}{\partial T}\Delta(T)\%$ = 8.14 % per unit Kelvin at T = 295.15 K. The Type B uncertainty in temperature that originates from calibration source, $\frac{\partial n}{\partial T}u_{cal}(T)$ is used to calculate the contribution of the uncertainty in n using above sensitivity relation (Eq. S3). The contribution

of the temperature data variability to *n* is already included in the spectral fit data variability and is therefore not separately calculated.

Table S4.I. The number density combined standard relative uncertainty budget.

Row	Contributing term		Hg	Hg-Air	Hg-N_2	Type
1	Path length (l), $\frac{u(l)}{l}\%$		0.062	0.122	0.141	B
2	[a]Temperature, T (K), $\frac{u(T)}{T}\%$	dataset variability	0.034	0.016	0.032	A
		thermometer calibration $\frac{u_{cal}(T)}{T}\%$	0.019	0.019	0.019	B
		Combined $\frac{u_c(T)}{T}\%$	0.039	0.025	0.037	-
3	Einstein coefficient, $\frac{u(A_{21})}{A_{21}}\%$		0.4	0.4	0.4	B
4	Spectral fit $m = nA_{21}l$ dataset variability, $\left(\left[\frac{u(m)}{m}\right]\% = \frac{u(n)}{n}\%\right)_{\chi_i, A_{21}, l=const}$		1.2	1.4	0.6	A
5	Spectral fit dependence on isotope abundance, $\frac{\left(\frac{\Delta(m[\chi_i])}{\Delta\chi_i}\right)u(\chi_i)}{m[\chi_i]}\%$, estimated		0.1	0.2	0.2	B
6	Spectral fit dependence on T, $\left(\frac{\frac{\Delta m}{\Delta T}}{m}\right)u_c(T)\%$		0.03	0.03	0.03	A
7	Number density dependence on T, $\frac{\frac{\partial n}{\partial T}}{n}u_{cal}(T)$ (%)		0.5	0.5	0.5	B
8	combined standard relative uncertainty, $\frac{u_c(n)}{n}\%$		1.3	1.5	0.9	-

[a]The contribution of temperature to the overall uncertainty is provided in rows 3 and 4 and is via the spectral fit dependence and number density dependence, respectively. The relative combined uncertainty $\frac{u_c(n)}{n}\%$ in row 8 is obtained by adding terms indicated in rows 1,3-7 in quadrature.

Supporting Information References

(1) Kramida, A. *Journal of Research of the National Institute of Standards and Technology* **2011**, *116*, 599-619.
(2) Schweitzer, W. G. *Journal of the Optical Society of America* **1963**, *53*, 1055-&.
(3) Bitter, F. *Applied Optics* **1962**, *1*, 1-10.
(4) Almog, G.; Scholz, M.; Weber, W.; Leisching, P.; Kaenders, W.; Udem, T. *Rev. Sci. Instrum.* **2015**, *86*, 5.
(5) Callear, A. B.; Patrick, C. R.; Robb, J. C. *Transactions of the Faraday Society* **1959**, *55*, 280-287.
(6) Granite, E. J.; Pennline, H. W. *Ind. Eng. Chem. Res.* **2002**, *41*, 5470-5476.
(7) Granite, E. J.; Pennline, H. W.; Hoffman, J. S. *Ind. Eng. Chem. Res.* **1999**, *38*, 5034-5037.